

# Multiplicity of Solar X-Ray Corona in Time and Space

R. KANO and the XRT team

*National Astronomical Observatory of Japan, 2-21-1 Osawa, Mitaka, Tokyo 181-8588, Japan*

(Received 5 January 2007 / Accepted 30 May 2007)

The Soft X-ray Telescope (XRT) aboard the Hinode satellite is a grazing incidence X-ray telescope equipped with  $2\text{ k} \times 2\text{ k}$  CCD. XRT has 1 arcsec resolution with wide field-of-view of  $34 \times 34$  arcmin. It is sensitive to  $< 1\text{ MK}$  to  $30\text{ MK}$ , allowing us to obtain TRACE-like low temperature images as well. Co-alignment with SOT and EIS is realized through the XRT visible light telescope and with temperature overlap with EIS. Spacecraft mission data processor (MDP) controls XRT through the sequence tables with versatile autonomous functions such as exposure control, region-of-interest tracking, flare detection and flare location identification. Data is compressed either with DPCM or JPEG, depending on the purpose. This results in higher cadence and/or wider field-of-view for given telemetry bandwidth. With focus adjust mechanism, higher resolution of Gaussian focus may be available on-axis.

© 2007 The Japan Society of Plasma Science and Nuclear Fusion Research

Keywords: solar corona, soft x-ray, grazing incidence telescope, back-illuminated ccd, high spatial resolution

DOI: 10.1585/pfr.2.S1010

## 1. Introduction

The Hinode satellite was launched on September 23, 2006. Its primary purpose is to observe the generation, transport, and emergence of solar magnetic fields, and ultimate dissipation of magnetic energy in a form such as flares and pico-flares, coronal heating, coronal mass ejection [1, 2]. The X-Ray Telescope (XRT) [3] aboard Hinode observes the dissipation part of the life-cycle story of solar magnetic fields. High-resolution soft X-ray images would reveal magnetic field configuration and its evolution, allowing us to observe the energy buildup, storage and release process in the corona for any transient event. One of the unique features of XRT is its wide temperature coverage to see all the coronal features, which are not seen with any normal incidence telescope. Though we recognize the limitation of the filter-ratio method, we point out that coronal structures and events such as magnetic reconnection are sometimes more clearly seen in the temperature maps than in the X-ray maps [4, 5].

XRT consists of the X-ray and visible light optics, focal plane mechanisms (filters and shutter), and the  $2\text{ k} \times 2\text{ k}$  CCD camera. The Mission Data Processor (MDP) also plays a vital role for XRT. XRT is the result of the Japan-US collaboration involving Smithsonian Astrophysical Observatory (SAO) under NASA MSFC (X-ray and visible-light optics), Institute of Space and Astronautical Science, Japan Aerospace Exploration Agency, and the National Astronomical Observatory of Japan (X-ray CCD camera and the MDP).

## 2. Instruments

Scientific requirements for the XRT are essentially summarized as follows: (1) Spatial resolution should be as close to or better than the X-ray/EUV telescopes in orbit as possible. (2) XRT should have field-of-view as wide as possible to see both the local and global phenomena. (3) XRT should have temperature range as wide as possible to see all the temperature components in the solar corona. In particular, it should have sensitivity in temperatures, to which Yohkoh/SXT was blind [6]. We chose grazing incidence optics for the Hinode XRT. A dominant factor leading to the decision was the wide temperature range that the grazing incidence optics brings us.

Grazing incidence optics has no inherent limitation on the wavelength sensitivity. XRT utilizes a back-illuminated CCD to enhance the sensitivity of longer wavelengths as compared with Yohkoh/SXT, which has a front-illuminated CCD. This essentially makes XRT TRACE-like when we have thin filters and SXT-like when we have thick filters as far as temperature sensitivity is concerned. We, however, need to be careful on what we are supposed to see. What we will see with this telescope is somewhat unknown, depending on the differential emission measure within a pixel.

### 2.1 X-ray and visible-light optics

XRT has soft X-ray and visible light (G-band) optics with common CCD (Figure 1). Both the X-ray and G-band images are focused on a single CCD. Either X-ray or visible-light images are selected by putting either a metal or a glass filter on the rotation filter wheel. The configuration is the same as SXT [9]. The visible light images of the Yohkoh SXT were so powerful for precise alignment of the

author's e-mail: ryouhei.kano@nao.ac.jp

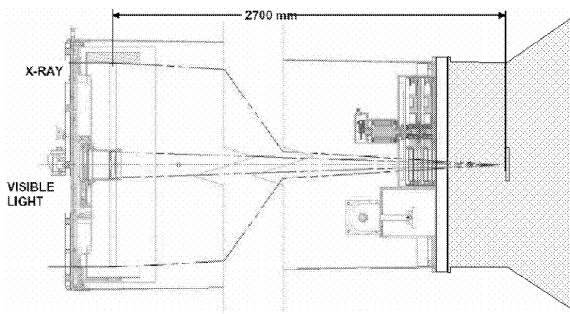


Fig. 1 XRT optical layout.

Table 1 XRT Characteristics.

X-Ray Optic	
Optic Design	optimized Wolter-I grazing incidence optics
Spatial Resolution	encircled energy of 68% within 2 arcsec @ 0.523 keV
Focal Length	2708 mm
Micro-Roughness	6 Å (expected)
Aperture Size	> 340 mm
Band Width	2 ~ 200 Å
Effective Area	> 1.0 cm <sup>2</sup> @ 0.523 keV
Visible Light Optic	
Focal Length	2708 mm
Wavelength	4305 Å (G-band)
Field of View	> 30 arcmin
Camera Performances	
CCD Type	Back-illuminated CCD (E2V/CCD 42-40)
Pixel Format	2048 × 2048 pixels
Pixel Size	13.5 × 13.5 μm (= 1 × 1 arcsec)
Field of View	34 × 34 arcmin
Pixel Binning Mode	1 × 1, 2 × 2, 4 × 4 and 8 × 8
Dark Current	0.1 e <sup>-</sup> /sec/pixel @ -65°C
CCD Temperature	passive cooling: < -43°C
CTE	Parallel > 0.999996, (-93°C < T < -50°C) Serial > 0.999999
QE (X-ray/EUV)	0.93 @ 13 Å, 0.61 @ 45 Å, 0.46 @ 116 Å, 0.56 @ 304 Å
QE (Visible Light)	0.44 @ 4000 Å, 0.66 @ 5000 Å
Full-well Capacity	2.0 × 10 <sup>5</sup> e <sup>-</sup>
System Gain	57 e <sup>-</sup> /DN
System Noise	< 30 e <sup>-</sup>
Output Data Bit	12 bit

X-ray images with any other images. This unique arrangement was repeated here to align the XRT images with other images. The parameters of X-ray and visible light optics are shown in Table 1.

### 2.2 X-ray analysis filters

XRT has two filter wheels for X-ray analysis filters and a G-band filter. These filter wheels have total of 10 po-

Table 2 Design of X-ray analysis filters.

Name	Metal	Substrate
Thin-Al/Mesh	Al	1600 Å Mesh
Thin-Al/Poly	Al	1250 Å Polyimide
C/Poly	C	6000 Å Polyimide
Ti/Poly	Ti	3000 Å Polyimide
Thin-Be	Be	9 μm
Med-Be	Be	30 μm
Med-Al	Al	12.5 μm
Thick-Al	Al	25 μm
Thick-Be	Be	300 μm

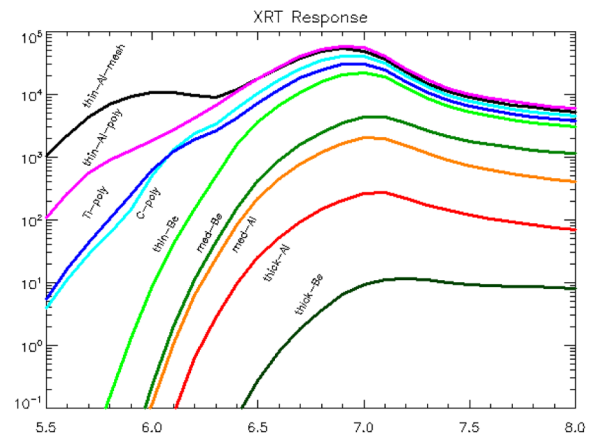


Fig. 2 Temperature response functions.

sitions; nine for the X-ray analysis filters and one for the visible-light filter. The X-ray analysis filters for the XRT are listed in Table 2. It is optimized to provide temperature maps over the range of 6.1 < log T < 7.5. Figure 2 shows the temperature response functions of the telescope including the entrance filter, the effective area of the X-ray mirror, and the measured quantum efficiency of the flight CCD.

### 2.3 CCD camera

XRT uses a back-illuminated three-phase CCD with 13.5 μm pixel-size and 2048 × 2048 array, which was manufactured by E2 V Technologies. The CCD will be operated under -43°C on the orbit. In Table 1, camera performances (mostly measured) are tabulated.

A unique feature of XRT is that the CCD is mounted on an adjustable (by command from the ground) stage with stroke of ±1 mm along the optical axis, while maintaining the stringent cooling requirement. This eliminates the risk of defocus in orbit, which would otherwise be difficult to overcome given the size and the complexity of the X-ray telescope. This design was driven by consideration of risk mitigation. However, this can be used in the scientific operation. Image plane of the grazing incidence optics is heavily curved, and the focus adjustment allows us to

choose either on-axis maximum resolution with rapid off-axis degradation (Gaussian focus) or the focus position that gives resolution as uniform as possible over a larger field-of-view.

XRT can take partial frame images for higher cadence. The horizontal and vertical size of the partial frame images are 64, 128, 192, 256, 384, 512, 768, 1024, 1536 and 2048, pixels. We select not only a square-shaped but also a rectangular-shaped partial frame image (ex.  $1024 \times 256$ ,  $256 \times 512$ ). Size of 64 pixels is, however, used only for square images ( $64 \times 64$ ). If the spacecraft is pointed to the center of the solar disk, the largest field-of-view ( $2048 \times 2048$  pixel =  $34 \times 34$  arcmin) can cover the full solar disk.

### 3. Observation Control Systems

XRT is scientifically controlled by the Mission Data Processor (MDP). MDP has a capability to perform on-board processing of the XRT image data for autonomous operation such as the selection for regions of interest (Automatic Region Selector; ARS, Automatic Exposure Control; AEC, and Flare Detection; FLD). MDP also has a dedicated pre-flare buffer.

#### 3.1 Observation tables

The MDP controls the XRT based on the observation tables stored inside MDP. The observation tables consist of three hierarchies of tables; main programs, subroutines and sequence tables.

Each sequence table includes eight exposure commands at maximum, and will be prepared as an elemental set of the XRT observations. For example, one sequence table may be designed for the full-disk temperature analysis with two alternate filters, and another for the DEM analysis with eight different filters in succession.

The sequence tables are building blocks for the main programs and subroutines. Observers will prepare the main programs and subroutines by combining the existing or newly uploaded sequence tables for their proposed observations. They need to upload the main program for flare observations that is activated when the flare flag is set by the Flare Detection logic.

#### 3.2 Automatic Exposure Control (AEC)

X-ray luminosity of the corona ranges over eight orders of magnitudes from coronal holes and outer corona to intense X-class flares, though the CCD has a dynamic range of three orders of magnitudes. Often the coronal intensity changes rapidly when flares start. Proper exposure is realized by changing the exposure duration over wide range. The Automatic Exposure Control (AEC) adjusts the exposure duration by analyzing the just-taken X-ray images onboard in pipe-line manner. (AEC is available only for the image with size smaller than 256 k pixels (i.e.  $512 \times 512$  pixel image).) If an X-ray image does

not achieve the proper exposure with the shortest exposure, AEC automatically changes the X-ray analysis filter to the thicker filter pre-specified (from the ground) in the observation table.

Note that AEC can be disabled for any exposure in the observing tables. It is also possible to intentionally take over or under exposure images for any exposure by changing the AEC parameters. This is sometimes very useful as demonstrated by Yohkoh.

#### 3.3 Automatic Region Selector (ARS)

The Automatic Region Selector (ARS) is the function to search the bright regions and to automatically update observing regions of the partial frame images. For this purpose, XRT takes full frame CCD images with an 8 arcsec resolution (ARS patrol images) at regular interval. The time resolution of the ARS depends on time resolution of ARS patrol images that can be set in the table. The baseline of the ARS time resolution is about 1.5 hour.

There are global search and local search modes in ARS. The global search selects the brightest region in the field-of-view. The local search tracks a bright region by searching only around the current location. There are 16 observing region target registers in the MDP to specify the locations of XRT observing regions. One of these is updated by the ARS global search, three by the ARS local search, ten by the ground command, and two by the flare detection, which will be described in the subsequent section.

#### 3.4 Flare Detection (FLD)

Hinode has no independent X-ray detection system dedicated to identifying solar flares. Thus the XRT has to do this by itself utilizing Flare Detection algorithm. Flare Detection (FLD) automatically identifies the occurrence of a flare, then determines the position on CCD, and finally issues a flare flag to the XRT as well as to the Solar Optical Telescope (SOT) and the EUV Imaging Spectrometer (EIS). To accomplish this, the XRT takes full frame CCD images with an 8-arcsec resolution (referred as FLD patrol images) at regular intervals. The baseline of FLD patrol interval is about 30 sec.

The method to identify flares is not based on a simple intensity threshold monitoring of FLD patrol images. Since many solar flares are generally not so bright at the beginning in soft X-rays, if flares are to be detected as soon as they occur, a simple threshold-based detection algorithm does not suffice. A better FLD algorithm is to monitor the increase in intensity by comparing with a running-averaged patrol image generated based on a collection of FLD patrol images taken previously. MDP calculates the parameter  $q^2$ , which is actually a map to show an increase

of the X-ray intensity normalized by the photon noise:

$$q^2 = \begin{cases} \frac{\{F - F_{\text{avg}}^{(i-1)}\}^2}{F_{\text{avg}}^{(i-1)} + g} & \text{for } F > F_{\text{avg}}^{(i-1)}, \\ 0 & \text{for } F < F_{\text{avg}}^{(i-1)}, \end{cases} \quad (1)$$

where  $g$  is a control parameter to avoid the division by 0,  $F$  is the patrol image to be evaluated, and  $F_{\text{avg}}^{(i)}$  is the running-averaged patrol image calculated by

$$F_{\text{avg}}^{(i)} = \gamma \cdot F + (1 - \gamma) \cdot F_{\text{avg}}^{(i-1)}, \quad (2)$$

where  $\gamma$  is also a parameter, which controls the effective duration of the running average. If  $q^2$  exceeds a threshold for flare start, MDP set the flare flag and find a flare location around the peak of  $q^2$ . The flare location will be dynamically stored in the last two of the observing region target registers, which is used in the observing sequence. When  $q^2$  becomes lower than a threshold for flare end, MDP drops the flare flag.

FLD also has a capability of the detection of radiation belts. In radiation belts, MDP changes the parameters of the flare detection algorithm to avoid the effect of the charged particles.

### 3.5 Image compression

The CCD video signal is digitized with 14 bit AtoD converter. The upper 12 bit is sent to MDP from the camera. Observers can specify three type of compression for each exposure in the observing tables; no compression, loss-less compression and lossy compression. In the no-compression mode, MDP is transparent. In the loss-less compression, MDP compress the image with the DPCM method which dose not loose any information of the image. The efficiency of DPCM for XRT images is expected about 50% (i.e. 6 bit/pixel) according to the simulation. This would become a popular option to reduce the amount of telemetry data. In the lossy compression, MDP compresses the image with JPEG method. It may be useful to provide context images for SOT and EIS and to perform purely morphological studies.

## 4. Initial Results of XRT

Since October in 2006, XRT started the initial observation. Figure 3 shows images taken with Thin-Al/Poly filter during the initial observation period. Many X-ray bright points (XBPs) were observed anywhere on the solar disk. With the high resolution of XRT, most of XBPs are seen as loops. XRT clearly shows the solar corona is filled with many loop structures not only in active regions but also in quiet Sun. XRT also observed many transient events; flares, micro flares and jets. XRT is a powerful telescope to reveal the coronal heating mechanism with SOT and EIS.

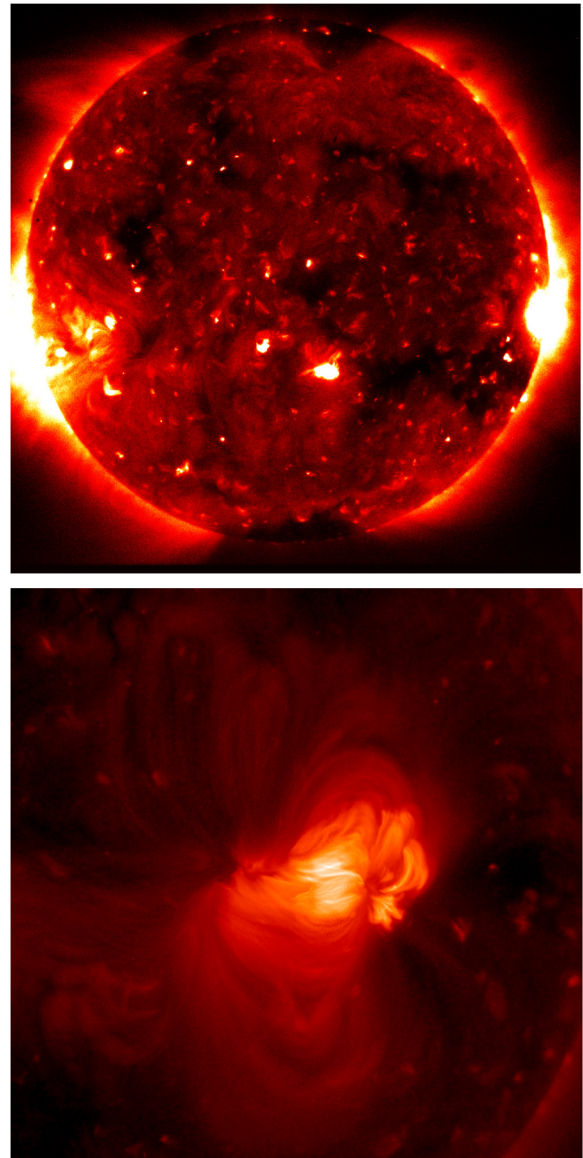


Fig. 3 Images taken with XRT. (upper) A full disk image taken at the beginning. (lower) A partial frame image around an active region.

We would like to thank our scientific and engineering colleagues of XRT. We also would like to thank the developing team of the MDP (MHI, SEC and ISAS).

- [1] Y. Katsukawa, Ph.D. thesis, Univ. of Tokyo (2004).
- [2] M. Kubo, T. Shimizu and B.W. Lites, *Astrophys. J.* **595**, 465 (2003).
- [3] L. Golub *et al.*, *Phys. Plasmas* **6**, 2205 (1999).
- [4] T. Yoshida and S. Tsuneta, *Astrophys. J.* **459**, 342 (1996).
- [5] R. Kano and S. Tsuneta, *PASJ* **48**, 535 (1996).
- [6] S. Nagata *et al.*, *Astrophys. J.* **590**, 1095 (2003).
- [7] L. Golub *et al.*, *Proc. SPIE* **4139**, 313 (2000).
- [8] C. Schrijver *et al.*, *Solar Phys.* **187**, 261 (1999).
- [9] S. Tsuneta *et al.*, *Solar Phys.* **136**, 37 (1991).